# Time-resolved x-ray scattering from impulsively aligned or oriented molecules

Mats Simmermacher [1,*] Adam Kirrander [1] and Niels E. Henriksen [2,†]
[1] *EaStCHEM, School of Chemistry, University of Edinburgh, EH9 3FJ Edinburgh, United Kingdom*
[2] *Department of Chemistry, Technical University of Denmark, 2800 Kongens Lyngby, Denmark*

(Received 4 September 2020; accepted 5 November 2020; published 23 November 2020)

Impulsive laser excitation of molecules can create rotational wave packets that lead to transient alignment or orientation. We present a theoretical analysis of the signatures of post-pulse field-free time-dependent alignment and orientation of diatomic molecules in time-resolved nonresonant x-ray scattering. This shows that alignment and its time dependence due to the interference terms of the rotational wave packet are visible in the x-ray scattering signal whereas signatures of orientation and its time dependence are absent. To that end, we discuss the time dependence of the coherent rotational motion associated with electronically resonant one-photon excitations. We illustrate our findings with calculated two-dimensional scattering signals for the sodium fluoride molecule (NaF) in the gas phase.

DOI: 10.1103/PhysRevA.102.052825

## I. INTRODUCTION

The real-time detection and control of molecular dynamics continues to be a topic at the forefront of modern chemical physics. Recent developments of x-ray free-electron lasers (XFELs) permit nonresonant x-ray scattering experiments for molecules in solution as well as in the gas phase [1–6]. Pump-probe setups with a time resolution below 100 fs allow for real-time tracking of structural dynamics.

A generic type of molecular dynamics is that of alignment or orientation, induced by the interaction of an ensemble of randomly oriented gas-phase molecules with the electric field of a laser pulse [7–13]. A sample of diatomic molecules AB is perfectly aligned if all the molecules are parallel to a space fixed axis, typically chosen as the polarization vector of the electric field. Orientation requires, in addition, that the atoms A point in the same direction. Impulsive laser excitation creates a rotational wave packet and post-pulse field-free alignment or orientation will occur in a periodic manner due to wave-packet revivals.

Impulsive alignment, also referred to as nonadiabatic or dynamic alignment, has been studied extensively in experiments. In a recent state-of-the-art example, an unprecedented degree of field-free alignment of carbonyl sulfide (OCS) was detected with velocity map imaging of the ionic fragments of the dissociating molecule [14]. Impulsive alignment has also been detected using ultrafast electron diffraction on trifluoroiodomethane ($CF_3I$) [15] and carbon disulfide ($CS_2$) [16] and fully time-resolved detection of the rotational dynamics has been achieved in nitrogen molecules [17]. Moreover, static adiabatic alignment induced by pulses with longer duration has been demonstrated with x-ray scattering [18,19]. The benefits of alignment for a complete retrieval of three-dimensional structure of molecules in the gas phase are significant [20].

On the theoretical side, the group of Santra presented theoretical studies of x-ray scattering from laser-aligned molecules [21–24]. In addition to the development of the relevant theoretical expressions, extensive computational studies of scattering patterns were presented for both diatomic and polyatomic molecules. Most of the computational studies addressed static alignment but also included a case of impulsively aligned $Br_2$ molecules [22]. Finally, Debnarova *et al.* investigated the scattering signal from statically aligned stilbene [25].

Motivated by these advances, we analyze the generic features of field-free time-dependent alignment as well as orientation of diatomic molecules [9–11] and their signatures in time-resolved x-ray scattering. Our work emphasizes the distinction between alignment and orientation. The paper is organized as follows: In Sec. II, we develop the theoretical expressions for the x-ray scattering signal and Sec. III presents illustratory simulations of the total scattering signal for various rotational wave packets of sodium fluoride (NaF) as recorded on a two-dimensional detector. Finally, Sec. IV summarizes our results.

## II. THEORY

The theory of time-resolved x-ray scattering has been developed in step with the experimental XFEL facilities [21,26–35]. For the present purpose, the standard theory of time-resolved x-ray scattering based on the independent atom model (IAM) suffices. Though deviations from the IAM can reveal important electronic effects such as chemical bonding or electronic excitations [36,37], they do not concern the signatures of rotational alignment or orientation considered here. Thus, the electron density is expressed as a sum of free atomic densities and contributions from coherently populated electronic states [30,32–35] are neglected.

*m.simmermacher@ed.ac.uk
†neh@kemi.dtu.dk

 

The elastic component of the time-resolved differential x-ray scattering signal in units of the Thomson scattering cross section for a molecule in a nonstationary nuclear state of the electronic ground state can be written as [29]

$$\frac{d\sigma_{\rm el}}{d\Omega} = \int \tilde{\rho}(\boldsymbol{R}, t_{\rm p})|F(\boldsymbol{R}, \boldsymbol{q})|^2 d\boldsymbol{R}, \tag{1}$$

where $\tilde{\rho}(\boldsymbol{R}, t_{\rm p})$ is the convolution of the instantaneous distribution (probability density) of the nuclear positions $\rho(\boldsymbol{R}, t)$ with the intensity profile of the x-ray pulse centered at $t = t_{\rm p}$. $F(\boldsymbol{R}, \boldsymbol{q})$ is the molecular scattering amplitude or form factor, and $\boldsymbol{q}$ is the scattering vector, i.e., the difference between the wave vectors of the incident and scattered x-ray photons. Thus, according to Eq. (1), the time-resolved x-ray scattering signal can be interpreted in terms of the conventional form factor weighted by the density of nuclear positions at the time of probing. Within the IAM, the elastic scattering intensity for a diatomic molecule takes the form

$$|F(\boldsymbol{R}, \boldsymbol{q})|^2 = |f_1(q)|^2 + |f_2(q)|^2 + 2f_1(q)f_2(q)\,\mathrm{Re}[e^{i\boldsymbol{q}\cdot\boldsymbol{R}}], \tag{2}$$

where $\boldsymbol{R} = \boldsymbol{R}_1 - \boldsymbol{R}_2$ is the bond vector, $\boldsymbol{R}_1$ and $\boldsymbol{R}_2$ are the position vectors of atoms 1 and 2, and $f_i(q)$ is a real-valued atomic form factor where $q = |\boldsymbol{q}|$. With this approximation and for an instantaneous x-ray probe pulse, Eq. (1) becomes

$$\frac{d\sigma_{\rm el}}{d\Omega} = |f_1(q)|^2 + |f_2(q)|^2 + 2f_1(q)f_2(q)\,\mathrm{Re}\left[\int e^{i\boldsymbol{q}\cdot\boldsymbol{R}}\rho(\boldsymbol{R}, t_{\rm p})d\boldsymbol{R}\right] \tag{3}$$

using that $\rho(\boldsymbol{R}, t_{\rm p})$ is normalized.

Now, consider a diatomic molecule rotationally excited by a linearly polarized laser pulse. At low rotational angular momentum, we can neglect the coupling between rotational and vibrational motion [38] to write the instantaneous distribution of the bond vector as

$$\rho(\boldsymbol{R}, t_{\rm p})d\boldsymbol{R} = \chi(R)^2|\psi(\theta, t_{\rm p})|^2 R^2 dR \sin\theta d\theta d\phi \tag{4}$$

with $\chi(R) = u(R)/R$, where $u(R)$ is the vibrational wave function, to a good approximation given by a Gaussian centered around the equilibrium bond length $R = R_{\rm eq}$. In the rigid-rotor approximation, the integrand in Eq. (3) is nonzero only for $R = R_{\rm eq}$. The rotational wave packet $\psi(\theta, t_{\rm p})$ is a function of the polar angle $\theta$ between the bond axis and the polarization vector of the laser field $\boldsymbol{\mathcal{E}}$. Due to the conservation of the $M$ quantum number during excitation by linearly polarized light, there is no dependence on the azimuthal angle $\phi$. The field-free time evolution of the rotational wave packet can be expanded in terms of spherical harmonic eigenfunctions $Y_{J,M}(\theta, \phi)$ [10],

$$|\psi(\theta, t_{\rm p})|^2 = \sum_{J'} |c_{J'}|^2 |Y_{J',M}(\theta, \phi)|^2 + 2\sum_{J'}\sum_{J''>J'} |c_{J'}||c_{J''}|Y_{J',M}(\theta, \phi)Y^*_{J'',M}(\theta, \phi) \times \cos[\Delta E_{J',J''}t_{\rm p}/\hbar - \varphi_{J',J''}] \tag{5}$$

with $\varphi_{J',J''} = \arg(c_{J'}) - \arg(c_{J''})$ and $\Delta E_{J',J''} = hc\tilde{B}_e[J'(J'+1) - J''(J''+1)]$, where $\tilde{B}_e$ is the rotational constant in wave numbers.

The populations of the spherical harmonics in Eq. (5) depend on the laser pulse and the mode of excitation. Interaction via static-dipole coupling leads to resonant excitation whereas interaction via induced-dipole coupling (electron polarization) takes place as nonresonant excitation. The selection rules for these processes are, respectively, $\Delta J = \pm 1$ and $\Delta J = \pm 2$. Assume the molecule is initially in $J = 0$; the interaction with intense laser fields leads then, in the two cases described above, to the population of either odd or even $J$ states [11].

In order to evaluate the integral in Eq. (3), we expand the exponential [39]

$$e^{i\boldsymbol{q}\cdot\boldsymbol{R}} = 4\pi \sum_{l=0}^{\infty}\sum_{m=-l}^{l} i^l j_l(qR)Y^*_{l,m}(\alpha, \delta)Y_{l,m}(\theta, \phi) \tag{6}$$

where $i$ is the imaginary unit, $j_l(qR)$ is a spherical Bessel function, and $(q, \alpha, \delta)$ are the norm and the polar and azimuthal angles of the $\boldsymbol{q}$ vector in the laboratory frame.

We consider two simple examples now. First, we work out the result for a superposition of the $(J, M) = (0, 0)$ and $(J, M) = (1, 0)$ states, corresponding to the simplest type of time-dependent orientation. In this case, Eq. (5) takes the form

$$|\psi(\theta, t_{\rm p})|^2 = |c_0|^2|Y_{0,0}(\theta, \phi)|^2 + |c_1|^2|Y_{1,0}(\theta, \phi)|^2 + 2|c_1||c_0|Y_{0,0}(\theta, \phi)Y^*_{1,0}(\theta, \phi) \times \cos[\Delta E_{1,0}t_{\rm p}/\hbar - \varphi_{1,0}]. \tag{7}$$

The first two terms are static and the mixing with higher angular momentum states $|Y_{J,0}(\theta, \phi)|^2$ leads to alignment along the polarization vector $\boldsymbol{\mathcal{E}}$ of the laser field. Concerning the last term in Eq. (7), we note that, for a fixed orientation, $\theta \to \pi - \theta$ with $\theta \in [0, \pi]$ and $\phi \to \phi + \pi$ when $\phi \in [0, \pi]$ and $\phi \to \phi - \pi$ when $\phi \in [\pi, 2\pi]$ specifies the opposite orientation. Under such an inversion of the molecular axis, $Y_{J,0}(\theta, \phi)$ changes sign for odd $J$ whereas there is no change in sign for even $J$. This implies that the last term in Eq. (7) changes sign when $\theta \to \pi - \theta$. The term therefore corresponds to a time-dependent change in orientation where, in general, $|\psi(\theta, t_{\rm p})|^2 \neq |\psi(\pi - \theta, t_{\rm p})|^2$ [9,10].

Focusing on the time-dependent part of the signal, we use Eqs. (4), (6), and (7) to evaluate the integral over $\boldsymbol{R}$ in Eq. (3),

$$2f_1(q)f_2(q)\,\mathrm{Re}\left[\int e^{i\boldsymbol{q}\cdot\boldsymbol{R}}\rho(\boldsymbol{R}, t_{\rm p})d\boldsymbol{R}\right] = 8\sqrt{\pi}f_1(q)f_2(q)|c_1||c_0|j_1(qR_{\rm eq})\mathrm{Re}[iY^*_{1,0}(\alpha, \delta)] \times \cos[\Delta E_{1,0}t_{\rm p}/\hbar - \varphi_{1,0}] = 0, \tag{8}$$

where we applied the orthonormality of spherical harmonics,

$$\langle Y_{l',m'}|Y_{l,m}\rangle = \int_0^{\pi}\int_0^{2\pi} Y^*_{l',m'}(\theta, \phi)Y_{l,m}(\theta, \phi)\sin\theta d\theta d\phi = \delta_{ll'}\delta_{mm'}. \tag{9}$$

Thus, field-free transient orientation does not lead to time dependence in the x-ray scattering signal. This result can be explained as follows: From Eq. (2), we can deduce that $|F(\boldsymbol{R}, \boldsymbol{q})|^2 = |F(-\boldsymbol{R}, \boldsymbol{q})|^2$. The squared form factor is thus

independent of the molecular orientation. It is symmetric under inversion $\boldsymbol{R} \to -\boldsymbol{R}$ while the time-dependent part of the nuclear density in Eq. (7) is antisymmetric under the same operation. The product of the squared form factor and the time-dependent part of the nuclear density is therefore an odd function of $(\theta, \phi)$ and the corresponding integral in Eq. (1) has to vanish. This argument generally applies to all time-dependent cross terms with spherical Harmonics that differ by an odd number in $J$, i.e., to all dynamics associated with molecular orientation beyond this simple example.

Second, for a superposition of the $(J, M) = (0, 0)$ and $(J, M) = (2, 0)$ states, corresponding to the simplest type of time-dependent alignment, Eq. (5) takes the form

$$|\psi(\theta, t_\mathrm{p})|^2 = |c_0|^2 |Y_{0,0}(\theta, \phi)|^2 + |c_2|^2 |Y_{2,0}(\theta, \phi)|^2 + 2|c_2||c_0| Y_{0,0}(\theta, \phi) Y^*_{2,0}(\theta, \phi) \times \cos[\Delta E_{2,0} t_\mathrm{p}/\hbar - \varphi_{2,0}]. \quad (10)$$

Again, the first two terms are static and reflect alignment that depends on the magnitude of the second term. Since $Y^*_{2,0}(\theta, \phi)$ is even under inversion of $\theta$, the last term of Eq. (10) refers to a time-dependent change in the degree of alignment. Focusing on this part of the signal again, we use Eqs. (4), (6), and (10) and evaluate the integral in Eq. (3),

$$2 f_1(q) f_2(q)\, \mathrm{Re}\left[\int e^{i\boldsymbol{q}\cdot\boldsymbol{R}} \rho(\boldsymbol{R}, t_\mathrm{p}) d\boldsymbol{R}\right] = -8\sqrt{\pi} f_1(q) f_2(q) |c_2||c_0| j_2(qR_\mathrm{eq}) Y^*_{2,0}(\alpha, \delta) \times \cos[\Delta E_{2,0} t_\mathrm{p}/\hbar - \varphi_{2,0}]. \quad (11)$$

Thus, field-free changes in time-dependent alignment are visible in the x-ray scattering signal and the dependence on the polar angle $\alpha$ of the $\boldsymbol{q}$ vector shows that the scattering pattern can appear anisotropically on the detector.

For a general rotational wave packet beyond the two examples discussed above, the integral in Eq. (3) can be written as

$$2 f_1(q) f_2(q) \mathrm{Re}\left[\int e^{i\boldsymbol{q}\cdot\boldsymbol{R}} \rho(\boldsymbol{R}, t_\mathrm{p}) d\boldsymbol{R}\right] = 8\pi f_1(q) f_2(q) \mathrm{Re}\left[\sum_{l=0}^{\infty} \sum_{m=-l}^{l} i^l Y^*_{l,m}(\alpha, \delta) \int_0^\infty j_l(qR) \left|\frac{u(R)}{R}\right|^2 R^2 dR \times \left(\sum_{J'} \sum_{M} |c_{J'}|^2 \int_0^\pi \int_0^{2\pi} Y_{l,m}(\theta, \phi) |Y_{J',M}(\theta, \phi)|^2 \sin\theta d\theta d\phi + 2 \sum_{J'} \sum_{J''>J'} \sum_{M} |c_{J'}||c_{J''}| \cos\left[\Delta E_{J',J''} t_\mathrm{p}/\hbar - \varphi_{J',J''}\right] \times \int_0^\pi \int_0^{2\pi} Y_{l,m}(\theta, \phi) Y_{J',M}(\theta, \phi) Y^*_{J'',M}(\theta, \phi) \sin\theta d\theta d\phi\right)\right]. \quad (12)$$

In Eq. (12), it is still assumed that $\Delta M = 0$ is fulfilled. We used the expansions of both the exponential, Eq. (6), and of a general rotational wave packet for a linear molecule that extends Eq. (5) such that an additional sum over quantum number $M$ is introduced. We have split the equation into diagonal and off-diagonal terms, the former with $J' = J''$ and the latter with $J' \neq J''$. These terms lead to, respectively, *static* and *time-dependent* contributions to the x-ray scattering signal. The sum over $M$ is bound to the interval $[-J',\ J']$ for $J' = J''$ and to $[-\min(J', J''),\ \min(J', J'')]$ for $J' \neq J''$.

Approximating the vibrational density $|u(R)|^2$ simply by a Dirac delta function around the equilibrium bond length $R_\mathrm{eq}$, we may write for the integral over $R$ in Eq. (12)

$$\int_0^\infty j_l(qR) \left|\frac{u(R)}{R}\right|^2 R^2 dR = \int_0^\infty j_l(qR) |u(R)|^2 dR \approx \int_0^\infty j_l(qR) \delta(R - R_\mathrm{eq}) dR = j_l(qR_\mathrm{eq}). \quad (13)$$

The integrals over the product of three spherical harmonics in Eq. (12) can be furthermore evaluated analytically in terms of Clebsch-Gordan coefficients $\langle j_1, m_1, j_2, m_2 | j_3, m_3 \rangle$ [39]

$$\int_0^\pi \int_0^{2\pi} Y_{l,m}(\theta, \phi) Y_{J',M}(\theta, \phi) Y^*_{J'',M}(\theta, \phi) \sin\theta d\theta d\phi = \sqrt{\frac{(2l+1)(2J'+1)}{4\pi(2J''+1)}} \langle J', 0, l, 0 | J'', 0\rangle \langle J', M, l, m | J'', M\rangle. \quad (14)$$

The Clebsch-Gordan coefficients require that the triangular condition, $|J' - J''| \leqslant l \leqslant J' + J''$, is fulfilled and that $m = 0$. The infinite sums over $l$ and $m$ in Eq. (12) thus truncate accordingly.

## III. SIMULATIONS AND DISCUSSION

To illustrate the findings discussed in Sec. II, we have simulated total x-ray scattering signals for sodium fluoride (NaF) in the gas phase as recorded on a two-dimensional detector. The signals are given in units of the Thomson scattering cross section throughout and are calculated for an equilibrium bond length of $R_\mathrm{eq} \approx 1.93$ Å and various rotational eigenstates and wave packets as specified below. The signals include the elas-

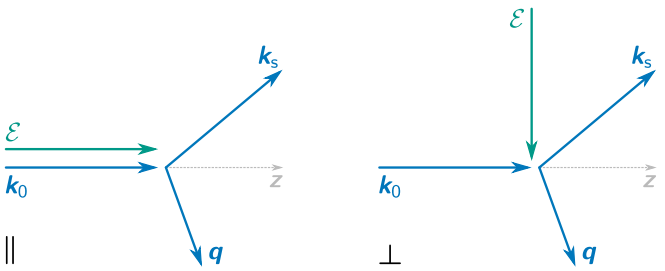


FIG. 1. Sketches of the collinear (∥) and perpendicular (⊥) pump-probe setups, defined by the relative orientation of the pump and the probe pulses. Here, $\boldsymbol{\mathcal{E}}$ is the polarization vector of the optical pump pulse and $\boldsymbol{k}_0$ is the wave vector of the incident x-ray photon, i.e., the probe pulse. Moreover, $\boldsymbol{k}_s$ illustrates the wave vector of a scattered photon and $\boldsymbol{q}$ is the corresponding momentum transfer (or scattering) vector. The $\boldsymbol{z}$ refers to the $z$ axis in the laboratory frame.

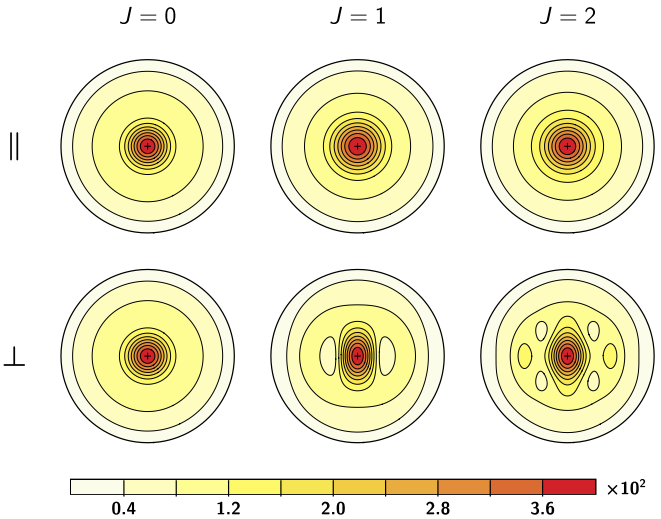


FIG. 2. Detector images of the *static* total x-ray scattering signal for sodium fluoride in three rotational eigenstates with quantum numbers $J \in \{0, 1, 2\}$ (all $M = 0$). The patterns are calculated in the $q_x$-$q_y$ plane for the collinear (∥) and perpendicular (⊥) pump-probe setups (see Fig. 1). The independent atom model and a mean x-ray photon energy of $c\hbar k_0 = 12.00$ keV are used. The radial coordinate of the detector takes values of $0 \leqslant q_{xy} \leqslant 6.081$ Å$^{-1}$. The scattering intensity is given in units of the Thomson scattering cross section, $(d\sigma/d\Omega)_{\mathrm{Th}}$. Note that the isotropic patterns of the collinear pump-probe setup are almost identical. The rotational eigenstates are distinguishable primarily by their anisotropic scattering patterns measured with the perpendicular pump-probe setup.

tic as well as the inelastic component, all calculated by means of the independent atom model with atomic form factors and incoherent scattering functions taken from the International Tables for Crystallography (see Tables 6.1.1.4 and 7.4.3.2 in Ref. [40]). Note that the inelastic component is described as an incoherent and structure-independent sum of the incoherent scattering functions of the two atoms. It is therefore also independent of time.

With the propagation of the incident x-ray pulse in the $z$ direction, the scattering patterns are calculated in the $q_x$-$q_y$ plane of the detector. They are evaluated on a three-dimensional $\boldsymbol{q}$-space grid by defining a two-dimensional grid of concentric circles around the origin in the $q_x$-$q_y$ plane with 37729 points in total. Within the elastic (or Waller-Hartree) approximation, $k_s \approx k_0$, where $k_0$ and $k_s$ are the norms of the wave vectors of the incident and scattered photons, respectively, the third coordinate of the $\boldsymbol{q}$ vector, $q_z$, is given by [41]

$$q_z = k_0\left(1 - \sqrt{1 - \frac{q_x^2 + q_y^2}{k_0^2}}\right). \tag{15}$$

The radial coordinate (norm) of $\boldsymbol{q}$, i.e., the argument of the atomic form factors, is simply $q = (q_x^2 + q_y^2 + q_z^2)^{1/2}$. Using a mean x-ray photon energy of $c\hbar k_0 = 12.00$ keV, it follows that the maximum value of $q$ is 8.600 Å$^{-1}$ and that the projection of $\boldsymbol{q}$ upon the $q_x$-$q_y$ plane of the detector is 6.081 Å$^{-1}$ at most.

To account for different experimental pump-probe setups, we rotate the $\boldsymbol{q}$ vector around the laboratory $y$ axis while effectively keeping the molecule and thus the excited rotational wave packet fixed. The resulting polar and azimuthal angles of $\boldsymbol{q}$, $\alpha$, and $\delta$, are calculated accordingly as

$$\alpha = \arccos\left[\frac{q_z\cos\gamma - q_x\sin\gamma}{q}\right], \tag{16}$$

$$\delta = \arctan\left[\frac{q_y}{q_x\cos\gamma + q_z\sin\gamma}\right], \tag{17}$$

where $\gamma$ refers to the angle of the rotation around the $y$ axis. The scattering patterns are shown for the collinear (∥) and perpendicular (⊥) pump-probe setups (see Fig. 1). These setups are defined by their respective angle between the wave vector of the incident x-ray photon $\boldsymbol{k}_0$ and the polarization vector $\boldsymbol{\mathcal{E}}$ of the pulse that excites the rotational wave packet, i.e., the $z$ axis of the spherical harmonics.

In the first case (∥), the pump pulse is polarized parallel to the direction of the incident x-ray pulse ($z$ direction). In the second case (⊥), it is polarized in the orthogonal $x$ direction. As expected, the patterns are isotropic in the collinear case and anisotropic in the perpendicular case (see Figs. 2–5). The scattering patterns are also centrosymmetric. To that end, we note that the molecular form factor $F(\boldsymbol{R}, \boldsymbol{q})$ is a Fourier transform of the real-valued electron density, which leads to $|F(\boldsymbol{R}, \boldsymbol{q})|^2 = |F(\boldsymbol{R}, -\boldsymbol{q})|^2$ (Friedel's law), also fulfilled within the IAM in Eq. (2). Thus, Friedel's law ensures inversion symmetry in the three-dimensional space of the $\boldsymbol{q}$ vector. In the context of the time-resolved scattering signal in Eq. (1), $|F(\boldsymbol{R}, \boldsymbol{q})|^2$ is weighted with the nuclear density as prepared by the pump pulse. Thus, whether the condition for centrosymmetry on the two-dimensional detector, $d\sigma/d\Omega(q_x, q_y) = d\sigma/d\Omega(-q_x, -q_y)$, is fulfilled depends on the alignment of the molecule with respect to the detector. Noncentrosymmetric scattering patterns can be observed with a setup in between our parallel and perpendicular setups [21,41]. We note in passing that recently a different type of deviation from centrosymmetry has been predicted [42].

With typical rotational timescales of many picoseconds, any x-ray pulse duration shorter than a few hundred femtoseconds will not give rise to noticeable changes. Thus, the scattering signals correspond to an instantaneous x-ray probe, which justifies the omission of the convolution with the temporal pulse profile.

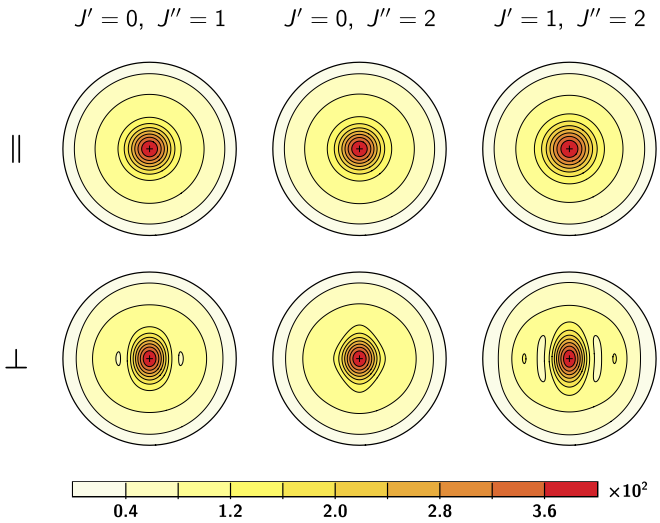


FIG. 3. Detector images of the *static* total x-ray scattering signal for sodium fluoride in three rotational wave packets. The wave packets contain two rotational eigenstates with different quantum numbers $J'$ and $J''$ each (all $M = 0$). The weights of the states are real valued and equal. The patterns are calculated in the $q_x$-$q_y$ plane for the collinear (∥) and perpendicular (⊥) pump-probe setups (see Fig. 1). The same method and parameters are applied as in Fig. 2.

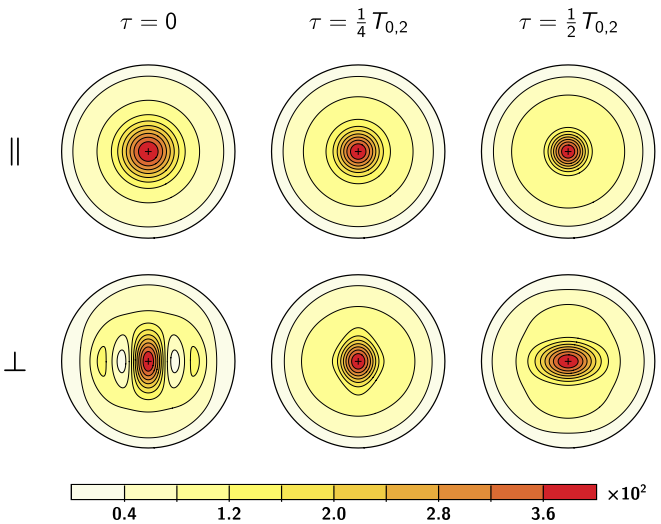


FIG. 4. Series of detector images at different pump-probe delay times $\tau$ of the *time-dependent* instantaneous total x-ray scattering signal for sodium fluoride in a rotational wave packet. The wave packet contains rotational eigenstates with quantum numbers $J' = 0$ and $J'' = 2$ (all $M = 0$). The weights of the states are real valued and equal. The patterns are calculated in the $q_x$-$q_y$ plane for the collinear (∥) and perpendicular (⊥) pump-probe setups (see Fig. 1). The pump-probe delay times $\tau$ are given in units of the rotational period of the wave packet, $T_{0,2} \approx 12.8$ ps. The same method and parameters are applied as in Fig. 2. Note that the patterns at $\tau = 3/4\ T_{0,2}$ and $\tau = T_{0,2}$ are not shown since they are identical to those at $\tau = 1/4\ T_{0,2}$ and $\tau = 0$, respectively. The time dependence of the signal is visible in both pump-probe setups and the pattern at $\tau = 1/4\ T_{0,2}$ is equal to the static signal (see Fig. 3, center column).

Turning to the numerical results, Fig. 2 shows static scattering patterns for individual rotational eigenstates with different quantum number $J$ (all $M = 0$). The $(J, M) = (0, 0)$ state corresponds to no alignment and the higher $J$ states imply an increasing degree of alignment. Figure 3 shows the static contribution to the scattering patterns of different rotational wave packets, i.e., signals arising from the time-independent part of Eq. (5). Each wave packet consists of two rotational states that contribute with equal weights, $c_i = 1/\sqrt{2}$. Again, alignment is visible as anisotropy in the perpendicular setup.

Figure 4 shows the total static plus time-dependent scattering signal at three different pump-probe delay times $\tau$ for a wave packet that consists of the two rotational states $(J, M) = (0, 0)$ and $(J, M) = (2, 0)$. Note that $\tau = t_p$ for a pump pulse centered at $t = 0$. Again, both states have equal weights, $c_i = 1/\sqrt{2}$, and since it is assumed that the coefficients are real valued the phase in Eq. (11) is $\varphi_{2,0} = 0$. The time is given in units of the period $T_{0,2} = h/\Delta E_{2,0}$. The time evolution of the signal reflects the change in the degree of alignment and is visible for both pump-probe setups. Using Eq. (12), the simulation presented in Fig. 4 can be easily extended to more complex wave packets that contain more than two rotational eigenstates, leading to scattering patterns that exhibit a richer and more intricate time dependence.

Typically, experimental pump-probe signals are reported as a difference signal ("pump on" minus "pump off"). To that end, Fig. 5 shows the difference scattering signal that corresponds to Fig. 4, that is, the signal in Fig. 4 minus the signal for the unaligned NaF molecule with an isotropic distribution ($J = 0$). Despite the simplicity of the model wave packet used here, the scattering patterns in Fig. 5 are qualitatively comparable to experimental electron diffraction patterns of a significantly more complex rotational wave packet of $N_2$ [17]. Quantifying the degree of alignment, $\langle\cos^2\theta\rangle$, the patterns at $\tau = 0$ can be related to the strongest alignment of the molecule along the polarization vector $\boldsymbol{\mathcal{E}}$, $\langle\cos^2\theta\rangle \approx 0.73$. The patterns at $\tau = 1/2\ T_{0,2}$, in contrast, re-

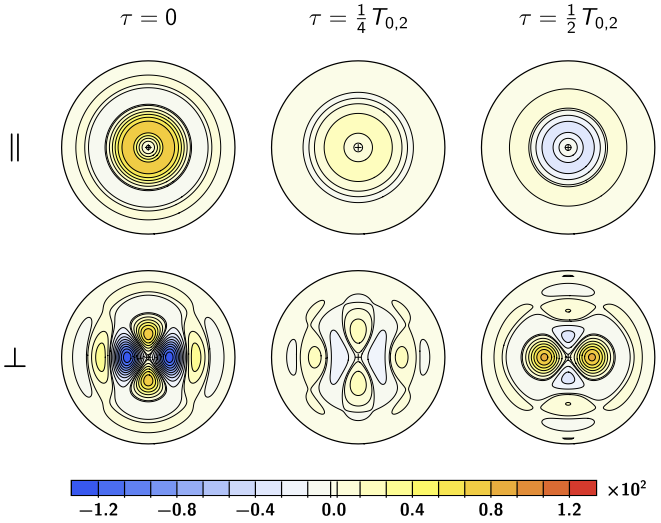


FIG. 5. Series of difference scattering patterns (pump on–pump off) that correspond to the detector images shown in Fig. 4. The static scattering signal for the rotational eigenstate with quantum numbers $(J, M) = (0, 0)$ (see Fig. 2, left column) is subtracted.

flect the molecule's strongest antialignment in a perpendicular direction, $\langle\cos^2\theta\rangle \approx 0.13$ (note that an isotropic ensemble of randomly oriented molecules shows $\langle\cos^2\theta\rangle = 1/3$ whereas $\langle\cos^2\theta\rangle = 1$ and $\langle\cos^2\theta\rangle = 0$ correspond to perfect alignment and antialignment, respectively). To realize a larger value of $\langle\cos^2\theta\rangle$ than observed in Fig. 5, one would need to increase the relative weight of the $(J, M) = (2, 0)$ state or to populate additional eigenstates with larger angular momentum quantum numbers $J$.

The two other wave packets displayed in Fig. 3 with $J_1 = 0$ and $J_2 = 1$ as well as $J_1 = 1$ and $J_2 = 2$, respectively, appear as completely static in the x-ray scattering signal. In line with the conclusion drawn from Eq. (8) before, their time-dependent contributions vanish. Thus, time-dependent changes in the orientation are not visible in time-resolved x-ray scattering. The observed signal is sensitive to molecular alignment but not to molecular orientation.

This result has important implications beyond the pure rotational excitations and assumptions discussed so far. Consider electronic coherences caused by an electronic transition in a diatomic molecule initially in its vibrational-rotational ground state. Within the electric-dipole approximation and first-order perturbation theory, the nuclear wave function of the electronically excited state is proportional to $\cos\theta$ and thus $Y_{1,0}(\theta, \phi)$ [29]. Transgressing the independent atom model, we can conclude that the interference terms between the initial $(J, M) = (0, 0)$ state and the excited $(J, M) = (1, 0)$ state do not add any time dependence to the scattering signal via its coherent mixed component and only static alignment is observed. Thus, if a change in the anisotropy is observed over time, it must be due to a change in the population of the excited $(J, M) = (1, 0)$ state, e.g., related to energy transfer to surrounding molecules. Again, we note that a description of coherent mixed scattering requires a theoretical framework that goes beyond the independent atom model applied here.

Electronic excitation can also create coherence between rotational eigenstates in the electronically excited state. Consider a molecule initially in a rotational state with $J \geqslant 1$ of the electronic ground state. Following the $\Delta J = \pm 1$ selection rule, both the $J + 1$ and the $J - 1$ states of the excited electronic state will become coherently populated. This coherence will add time dependence to the scattering signal (similar to Fig. 4). Furthermore, when we do not have an electronic $\Sigma \leftarrow \Sigma$ transition, $\Delta J = 0$ also applies, but due to the odd-valued differences in $J$ with the $J + 1$ and $J - 1$ states, respectively, the resulting coherences and time dependence of the rotational wave packet are not visible in the scattering signal. These conclusions are valid for the experimentally relevant case of a partially coherent rotational wave packet that was, prior to its excitation, thermally populated. Here, the time-dependent contributions to the scattering signal from coherently populated states (those that differ by $\Delta J = 2$ for $J \geqslant 1$) will be visible.

To that end, we also note that signatures of alignment due to photoexcitation have been detected and exploited in recent work that distinguished different excitation channels [43] and electronically excited states [44] by means of anisotropic electron and x-ray scattering, respectively. Furthermore, alignment is a prerequisite for the observation of interference between multiple coherently excited electronic states in time-resolved x-ray scattering when electronic coherences prepared by resonant one-photon excitation are probed [33]. The observation of these *coherent mixed* terms in homonuclear diatomic molecules requires some degree of alignment of the molecule. For a pure $(J, M) = (0, 0)$ state or an isotropic rotational density in general, the coherent mixed component averages out (see Ref. [33]). The $(J, M) = (1, 0)$ state that is excited by the pump pulse when the electronic coherence is created, however, allows for a nonvanishing contribution. How large that contribution is depends not only on the weight of the $(J, M) = (1, 0)$ state but also on properties of the molecule, pulse, and detector.

As the discussion above illustrates, our findings concerning the time dependence of the scattering signal have been demonstrated within the IAM but are applicable and valid beyond. This conclusion can be drawn from the general theory of time-resolved x-ray scattering [34].

## IV. SUMMARY

We consider the detection of rotational dynamics in diatomic or linear molecules via time-resolved nonresonant x-ray scattering. We find that if the wave packet consists of eigenstates that differ by an even number in $J$, rotational motion adds time dependence to the scattering signal, reflecting alignment and its field-free time evolution. If the wave packet consists of eigenstates that differ by an odd number in $J$, the time-dependent interference terms that lead to transient changes in molecular orientation do not affect the scattering signal. Both types of wave packets can be created experimentally, depending on the mode of interaction with the driving laser field.

We also discuss the time dependence associated with coherent rotational motion created by electronically resonant one-photon excitation driven by linearly polarized light, within the conditions imposed by the electric-dipole approximation and first-order perturbation theory. We point out that time-dependent contributions to the x-ray scattering signal originate from coherently populated rotational states that differ by $\Delta J = 2$.

Our theoretical and computational results point to an important distinction between alignment and orientation and how this manifests itself in the anisotropy of time-resolved x-ray scattering signals. This has immediate implications for experiments that wish to detect anisotropy in rotationally excited molecules, an aspect of time-resolved x-ray scattering that is bound to receive increasing attention in the coming years.

The data that support the findings of this study are available from the corresponding authors upon reasonable request.

[1] D. Arnlund, L. C. Johansson, C. Wickstrand, A. Barty, G. J. Williams, E. Malmerberg, J. Davidsson, D. Milathianaki, D. P. DePonte, R. L. Shoeman, D. Wang, D. James, G. Katona, S. Westenhoff, T. A. White, A. Aquila, S. Bari, P. Berntsen,

M. Bogan, T. B. van Driel, R. B. Doak, K. S. Kjær, M. Frank, R. Fromme, I. Grotjohann, R. Henning, M. S. Hunter, R. A. Kirian, I. Kosheleva, C. Kupitz, M. Liang, A. V. Martin, M. M. Nielsen, M. Messerschmidt, M. M. Seibert, J. Sjöhamn, F. Stellato, U. Weierstall, N. A. Zatsepin, J. C. H. Spence, P. Fromme, I. Schlichting, S. Boutet, G. Groenhof, H. N. Chapman, and R. Neutze, Visualizing a protein quake with time-resolved x-ray scattering at a free-electron laser, Nat. Methods **11**, 923 (2014).

[2] K. H. Kim, J. G. Kim, S. Nozawa, T. Sato, K. Y. Oang, T. W. Kim, H. Ki, J. Jo, S. Park, C. Song, T. Sato, K. Ogawa, T. Togashi, K. Tono, M. Yabashi, T. Ishikawa, J. Kim, R. Ryoo, J. Kim, H. Ihee, and S.-I. Adachi, Direct observation of bond formation in solution with femtosecond x-ray scattering, Nature (London) **518**, 385 (2015).

[3] M. Levantino, G. Schiró, H. T. Lemke, C. Grazia, J. M. Glownia, Z. Diling, M. Chollet, H. Ihee, A. Cupane, and M. Cammarata, Ultrafast myoglobin structural dynamics observed with an x-ray free-electron laser, Nat. Commun. **6**, 6772 (2015).

[4] T. B. van Driel, K. S. Kjær, R. W. Hartsock, A. O. Dohn, T. Harlang, M. Chollet, M. Christensen, W. Gawelda, N. E. Henriksen, J. G. Kim, K. Haldrup, K. H. Kim, H. Ihee, J. Kim, H. Lemke, Z. Sun, V. Sundström, W. Zhang, D. Zhu, K. B. Møller, M. M. Nielsen, and K. J. Gaffney, Atomistic characterization of the active-site solvation dynamics of a model photocatalyst, Nat. Commun. **7**, 13678 (2016).

[5] J. M. Budarz, M. P. Minitti, D. V. Cofer-Shabica, B. Stankus, A. Kirrander, J. B. Hastings, and P. M. Weber, Observation of femtosecond molecular dynamics via pump-probe gas phase x-ray scattering, J. Phys. B: At. Mol. Opt. Phys. **49**, 034001 (2016).

[6] M. P. Minitti, J. M. Budarz, A. Kirrander, J. S. Robinson, D. Ratner, T. J. Lane, D. Zhu, J. M. Glownia, M. Kozina, H. T. Lemke, M. Sikorski, Y. Feng, S. Nelson, K. Saita, B. Stankus, T. Northey, J. B. Hastings, and P. M. Weber, Imaging Molecular Motion: Femtosecond x-ray Scattering of an Electrocyclic Chemical Reaction, Phys. Rev. Lett. **114**, 255501 (2015).

[7] H. Stapelfeldt and T. Seideman, Colloquium: Aligning molecules with strong laser pulses, Rev. Mod. Phys. **75**, 543 (2003).

[8] C. Vallance, Generation, characterisation, and applications of atomic and molecular alignment and orientation, Phys. Chem. Chem. Phys. **13**, 14427 (2011).

[9] N. E. Henriksen, Molecular alignment and orientation in short pulse laser fields, Chem. Phys. Lett. **312**, 196 (1999).

[10] M. Machholm and N. E. Henriksen, Field-Free Orientation of Molecules, Phys. Rev. Lett. **87**, 193001 (2001).

[11] C. C. Shu and N. E. Henriksen, Field-free molecular orientation induced by single-cycle THz pulses: The role of resonance and quantum interference, Phys. Rev. A **87**, 013408 (2013).

[12] K. N. Egodapitiya, S. Li, and R. R. Jones, Terahertz-Induced Field-Free Orientation of Rotationally Excited Molecules, Phys. Rev. Lett. **112**, 103002 (2014).

[13] E. F. Thomas, A. A. Søndergaard, B. Shepperson, N. E. Henriksen, and H. Stapelfeldt, Hyperfine-Structure-Induced Depolarization of Impulsively Aligned $I_2$ Molecules, Phys. Rev. Lett. **120**, 163202 (2018).

[14] E. T. Karamatskos, S. Raabe, T. Mullins, A. Trabattoni, P. Stammer, G. Goldsztejn, R. R. Johansen, K. Długołecki, H. Stapelfeldt, M. J. J. Vrakking, S. Trippel, A. Rouzée, and J. Küpper, Molecular movie of ultrafast coherent rotational dynamics of OCS, Nat. Commun. **10**, 3364 (2019).

[15] C. J. Hensley, J. Yang, and M. Centurion, Imaging of Isolated Molecules with Ultrafast Electron Pulses, Phys. Rev. Lett. **109**, 133202 (2012).

[16] J. Yang, J. Beck, C. J. Uiterwaal, and M. Centurion, Imaging of alignment and structural changes of carbon disulfide molecules using ultrafast electron diffraction, Nat. Commun. **6**, 8172 (2015).

[17] J. Yang, M. Guehr, T. Vecchione, M. S. Robinson, R. Li, N. Hartmann, X. Shen, R. Coffee, J. Corbett, A. Fry, K. Gaffney, T. Gorkhover, C. Hast, K. Jobe, I. Makasyuk, A. Reid, J. Robinson, S. Vetter, F. Wang, S. Weathersby, C. Yoneda, M. Centurion, and X. Wang, Diffractive imaging of a rotational wavepacket in nitrogen molecules with femtosecond megaelectronvolt electron pulses, Nat. Commun. **7**, 11232 (2016).

[18] J. Küpper, S. Stern, L. Holmegaard, F. Filsinger, A. Rouzée, A. Rudenko, P. Johnsson, A. V. Martin, M. Adolph, A. Aquila, S. Bajt, A. Barty, C. Bostedt, J. Bozek, C. Caleman, R. Coffee, N. Coppola, T. Delmas, S. Epp, B. Erk, L. F. T. Gorkhover, L. Gumprecht, A. Hartmann, R. Hartmann, G. Hauser, P. Holl, A. Hömke, N. Kimmel, F. Krasniqi, K.-U. Kühnel, J. Maurer, M. Messerschmidt, R. Moshammer, C. Reich, B. Rudek, R. Santra, I. Schlichting, C. Schmidt, S. Schorb, J. Schulz, H. Soltau, J. C. H. Spence, D. Starodub, L. Strüder, J. Thøgersen, M. J. J. Vrakking, G. Weidenspointner, T. A. White, C. Wunderer, G. Meijer, J. Ullrich, H. Stapelfeldt, D. Rolles, and H. N. Chapman, X-ray Diffraction from Isolated and Strongly Aligned gas-Phase Molecules with a Free-Electron Laser, Phys. Rev. Lett. **112**, 083002 (2014).

[19] T. Kierspel, A. Morgan, J. Wiese, T. Mullins, A. Aquila, A. Barty, R. Bean, R. Boll, S. Boutet, P. Bucksbaum, H. N. Chapman, L. Christensen, A. Fry, M. Hunter, J. E. Koglin, M. Liang, V. Mariani, A. Natan, J. Robinson, D. Rolles, A. Rudenko, K. Schnorr, H. Stapelfeldt, S. Stern, J. Thøgersen, C. H. Yoon, F. Wang, and J. Küpper, X-ray diffractive imaging of controlled gas-phase molecules: Toward imaging of dynamics in the molecular frame, J. Chem. Phys. **152**, 084307 (2020).

[20] J. Yang, V. Makhija, V. Kumarappan, and M. Centurion, Reconstruction of three-dimensional molecular structure from diffraction of laser-aligned molecules, Struct. Dyn. **1**, 044101 (2014).

[21] P. J. Ho and R. Santra, Theory of x-ray diffraction from laser-aligned symmetric-top molecules, Phys. Rev. A **78**, 053409 (2008).

[22] P. J. Ho, M. R. Miller, and R. Santra, Field-free molecular alignment for studies using x-ray pulses from a synchrotron radiation source, J. Chem. Phys. **130**, 154310 (2009).

[23] P. J. Ho, D. Starodub, D. K. Saldin, V. L. Shneerson, A. Ourmazd, and R. Santra, Molecular structure determination from x-ray scattering patterns of laser-aligned symmetric-top molecules, J. Chem. Phys. **131**, 131101 (2009).

[24] S. Pabst, P. J. Ho, and R. Santra, Computational studies of x-ray scattering from three-dimensionally-aligned asymmetric-top molecules, Phys. Rev. A **81**, 043425 (2010).

[25] D. Debnarova, A. S. Techert, and S. Schmatz, Computational studies of the x-ray scattering properties of laser aligned stilbene, J. Chem. Phys. **134**, 054302 (2011).

[26] M. Ben-Nun, J. Cao, and K. R. Wilson, Ultrafast x-ray and electron diffraction: Theoretical considerations, J. Phys. Chem. A **101**, 8743 (1997).

[27] J. Cao and K. R. Wilson, Ultrafast x-ray diffraction theory, J. Phys. Chem. A **102**, 9523 (1998).

[28] N. E. Henriksen and K. B. Møller, On the theory of time-resolved x-ray diffraction, J. Phys. Chem. B **112**, 558 (2008).

[29] K. B. Møller and N. E. Henriksen, Time-resolved x-ray diffraction: The dynamics of the chemical bond, Struc. Bond. **142**, 185 (2012).

[30] G. Dixit, O. Vendrell, and R. Santra, Imaging electronic quantum motion with light, Proc. Natl. Acad. Sci. USA **109**, 11636 (2012).

[31] A. Kirrander, K. Saita, and D. V. Shalashilin, Ultrafast x-ray scattering from molecules, J. Chem. Theory Comput. **12**, 957 (2016).

[32] K. Bennett, M. Kowalewski, J. R. Rouxel, and S. Mukamel, Monitoring molecular nonadiabatic dynamics with femtosecond x-ray diffraction, Proc. Natl. Acad. Sci. USA **115**, 6538 (2018).

[33] M. Simmermacher, N. E. Henriksen, K. B. Møller, A. Moreno Carrascosa, and A. Kirrander, Electronic Coherence in Ultrafast x-ray Scattering from Molecular Wave Packets, Phys. Rev. Lett. **122**, 073003 (2019).

[34] M. Simmermacher, A. M. Carrascosa, N. E. Henriksen, K. B. Møller, and A. Kirrander, Theory of ultrafast x-ray scattering by molecules in the gas phase, J. Chem. Phys. **151**, 174302 (2019).

[35] G. Hermann, V. Pohl, G. Dixit, and J. C. Tremblay, Probing Electronic Fluxes Via Time-Resolved X-ray Scattering, Phys. Rev. Lett. **124**, 013002 (2020).

[36] T. Northey, N. Zotev, and A. Kirrander, *Ab initio* calculation of molecular diffraction, J. Chem. Theory Comput. **10**, 4911 (2014).

[37] H. Yong, N. Zotev, J. M. Ruddock, B. Stankus, M. Simmermacher, A. M. Carrascosa, W. Du, N. Goff, Y. Chang, D. Bellshaw, M. Liang, S. Carbajo, J. E. Koglin, J. S. Robinson, S. Boutet, M. P. Minitti, A. Kirrander, and P. M. Weber, Observation of the molecular response to light upon photoexcitation, Nat. Commun. **11**, 2157 (2020).

[38] C. C. Shu and N. E. Henriksen, Communication: Creation of molecular vibrational motions via the rotation-vibration coupling, J. Chem. Phys. **142**, 221101 (2015).

[39] G. B. Arfken, H. J. Weber, and F. E. Harris, *Mathematical Methods of Physicists*, 7th ed. (Academic Press, San Diego, 2012).

[40] A. J. C. Wilson and E. Prince, *International Tables for Crystallography*, Vol. C (Kluwer, Dordrecht, 1999).

[41] M. Simmermacher, Theory and simulations of time-resolved x-ray scattering, Ph.D. thesis, Technical University of Denmark, Kongens Lyngby, 2018.

[42] H.-C. Shao and A. F. Starace, Violation of centrosymmetry in time-resolved coherent x-ray diffraction from rovibrational states of diatomic molecules, Phys. Rev. A **99**, 033413 (2019).

[43] J. Yang, X. Zhu, T. J. A. Wolf, Z. Li, J. P. F. Nunes, R. Coffee, J. P. Cryan, M. Gühr, K. Hegazy, T. F. Heinz, K. Jobe, R. Li, X. Shen, T. Veccione, S. Weathersby, K. J. Wilkin, C. Yoneda, Q. Zheng, T. J. Martinez, M. Centurion, and X. Wang, Imaging $CF_3I$ conical intersection and photodissociation dynamics with ultrafast electron diffraction, Science **361**, 64 (2018).

[44] H. Yong, N. Zotev, B. Stankus, J. M. Ruddock, D. Bellshaw, S. Boutet, T. J. Lane, M. Liang, S. Carbajo, J. S. Robinson, W. Du, N. Goff, Y. Chang, J. E. Koglin, M. D. J. Waters, T. I. Sølling, M. P. Minitti, A. Kirrander, and P. M. Weber, Determining orientations of optical transition dipole moments using ultrafast x-ray scattering, J. Phys. Chem. Lett. **9**, 6556 (2018).